

# Beyond Linear Superposition: Discovering Climate Features in AI Weather Models with KAN-SAE

Minjong Cheon  
 Department of Computer Science and Engineering  
 Sejong University  
 jmj2316@sejong.ac.kr

May 19, 2026

## Abstract

Deep learning weather prediction models achieve remarkable predictive skill yet remain largely opaque: we know little about how they represent physical climate phenomena internally. Mechanistic interpretability through Sparse Autoencoders (SAEs) offers a principled route to decomposing these representations, but existing SAEs assume strictly linear feature superposition—a constraint ill-suited for the highly nonlinear atmospheric dynamics encoded in modern transformers. We introduce KAN-SAE, a sparse autoencoder whose encoder replaces the standard ReLU with learnable per-feature B-spline activations drawn from Kolmogorov–Arnold Networks (KANs), allowing each latent dimension to develop its own nonlinear gating profile. Applied to SONNY, KAN-SAE discovers 975 alive features (vs. 566 for a linear baseline, a 72% improvement) with 20% lower inter-feature redundancy and comparable reconstruction fidelity. Without any climate supervision, KAN-SAE identifies an interpretable European heatwave feature spatially concentrated over western Europe, and a western Pacific typhoon tracker confirmed by causal steering experiments. Our results demonstrate that nonlinear activations are essential for mechanistic interpretability of deep learning weather prediction models, recovering climate features that remain invisible to linear baselines.

Keywords: Feature Discovery; Kolmogorov-Arnold Networks; Mechanistic Interpretability; Sparse Autoencoders; Weather Forecasting

## 1 Introduction

Deep learning has rapidly reshaped weather prediction. Data-driven systems such as GraphCast [9], Pangu-Weather [1], and STORMER [14] now match or exceed strong operational baselines while requiring only a fraction of the computational cost of traditional physics-based pipelines. This progress has made deep learning weather prediction increasingly attractive for medium-range prediction, climate risk assessment, and rapid scenario analysis. Yet their predictive skill has not been matched by a comparable understanding of their internal representations. It remains unclear whether these models learn reusable physical concepts—such as blocking regimes, heatwave precursors, or tropical cyclone structures—or whether their forecasts arise from distributed statistical correlations that resist inspection and intervention. This opacity is especially consequential in meteorology, where forecast trust depends not only on aggregate error metrics but on whether a model’s internal reasoning is consistent with known atmospheric dynamics.

Mechanistic interpretability offers a principled route from opaque forecasting systems to models whose internal variables can be scientifically analysed. Sparse Autoencoders (SAEs) [2, 4] have emerged as a scalable method for decomposing neural network activations into a large dictionary of sparsely active, potentially interpretable features. The approach

rests on the *linear representation hypothesis* [5]: a network with  $d$  hidden dimensions can represent  $n \gg d$  latent features by linearly superposing them in activation space. Standard SAEs instantiate this assumption with a linear encoder, a ReLU bottleneck, and an  $\ell_1$  sparsity penalty, and have proved useful for language models where many features correspond to recognisable lexical or semantic concepts.

The linear superposition assumption, however, is less obviously appropriate for atmospheric representations. Climate and weather phenomena are inherently nonlinear: a blocking anticyclone is not simply “more blocking” because Z500 is higher; a jet stream displacement depends on direction and curvature as much as amplitude; and tropical cyclone structure involves thresholded, saturated, and spatially organised interactions across variables. A feature may be present only after an activation crosses a regime-dependent threshold, or it may saturate once a synoptic pattern has fully developed. Forcing all latent features through the same linear projection and a universal ReLU gate artificially constrains the expressiveness of the learned dictionary—manifesting in practice as dead neurons, redundant features, or feature directions that conflate several physical mechanisms.

In this paper, we propose KAN-SAE (Figure 1), a nonlinear sparse autoencoder that replaces the standard ReLU with a bank of learnable B-spline activation functions drawn from Kolmogorov–Arnold Networks [11], one per latent dimension. This modification preserves the sparse dictionary structure of SAEs while allowing each feature to learn its own gating profile—including sharp thresholds, saturation, asymmetric sensitivity, and non-monotone responses—at exactly the point where atmospheric regime changes are most likely to matter. Applied to SONNY [3] trained on ERA5 reanalysis, KAN-SAE discovers 95.2% of its dictionary as alive features (vs. 55.5% for a linear baseline) with 20% lower inter-feature redundancy and comparable reconstruction fidelity. Qualitative analysis reveals physically meaningful features including a European heatwave detector spatially concentrated over western Europe, and a western Pacific typhoon tracker confirmed by causal steering experiments.

Our main contributions are:

1. KAN-SAE, a nonlinear sparse autoencoder with per-feature learnable B-spline activations, designed for mechanistic interpretability of atmospheric transformers.
2. Empirical evidence that KAN-SAE learns a significantly richer and less redundant feature dictionary: 95.2% vs. 55.5% feature utilisation and 20% lower inter-feature correlation relative to a linear SAE under identical training conditions.
3. Discovery of physically interpretable climate features—a European heatwave detector spatially concentrated over western Europe, and a tropical cyclone tracker for the western Pacific—without any climate supervision.
4. Causal steering experiments confirming that individual features modulate downstream temperature forecasts by up to  $\pm 3$  K, with geographically localised effects consistent with the corresponding climate patterns.

## 2 Related Work

**Mechanistic interpretability and sparse autoencoders.** Mechanistic interpretability seeks to reverse-engineer the internal computations of neural networks by identifying interpretable circuits and features [15, 20]. A key challenge is *polysemanticity*—the tendency of individual neurons to respond to multiple unrelated concepts [5]. Bricken et al. [2] demonstrated that SAEs can decompose transformer residual stream activations into a large overcomplete dictionary of monosemantic features, and subsequent work has scaled this approach to frontier language models [19, 10]. The standard SAE encoder uses a linear projection followed by a ReLU bottleneck and an  $\ell_1$  sparsity penalty; variants include TopK activation [6] and gated encoders [21] to reduce dead features. In all cases, the encoder assumes that features are linearly separable in pre-activation space. Our work relaxes this assumption by equipping each latent dimension with a learnable B-spline function, targeting the nonlinear activation regimes characteristic of atmospheric phenomena.

**Interpretability of deep learning weather prediction models.** Modern deep learning weather prediction models [1, 9, 17, 13] match or exceed ECMWF operational skill at medium range, yet their internal representations remain poorly understood. Existing interpretability analyses focus predominantly on post-hoc attribution methods or attention-pattern visualisation [18], which characterise input–output sensitivity but do not reveal the latent feature structure organising model computations. MacMillan and Ouellette [12] is the closest prior work to ours: they train  $k$ -sparse SAEs on the intermediate node embeddings of GraphCast [9], uncovering features that correspond to tropical cyclones, atmospheric rivers, sea-ice extent, and diurnal and seasonal cycles, and demonstrate causal steering of hurricane intensity via direct feature modification. This work establishes the viability of SAE-based mechanistic interpretability for global deep learning weather prediction models and provides the strongest evidence that physically meaningful abstractions spontaneously emerge in data-driven forecasters. Our contribution is orthogonal: whereas MacMillan and Ouellette [12] apply a standard linear SAE to GraphCast, we ask whether the linear superposition assumption itself limits the richness of the discovered feature vocabulary. By replacing the universal ReLU with per-feature B-spline activations, KAN-SAE discovers a substantially larger and less redundant feature dictionary on SONNY [3], suggesting that the nonlinear gating structure of atmospheric phenomena is better captured by learned per-feature activation shapes than by a shared linear threshold.

**Kolmogorov–Arnold Networks.** KANs [11] replace the fixed weight matrices of multi-layer perceptrons with learnable univariate functions parameterised as B-splines, demonstrating competitive accuracy with fewer effective parameters on function-approximation benchmarks. The theoretical motivation is the Kolmogorov–Arnold representation theorem, which guarantees that any continuous multivariate function can be decomposed into a composition of univariate functions. Extensions have adapted KANs to scientific computing and physics-informed settings, exploiting the interpretability of the learned activation shapes. We do not adopt the full KAN architecture; instead, we transplant only its B-spline parameterisation as a per-feature activation function within the SAE encoder. This targeted borrowing preserves the sparse dictionary structure of SAEs—crucial for feature-level interpretability—while equipping each latent dimension with the flexibility to learn its own gating profile without increasing the decoder complexity.

## 3 Background and Preliminaries

### 3.1 Deep Learning Weather Prediction and SONNY

Deep learning weather prediction trains neural networks on historical reanalysis data to predict future atmospheric states, replacing the costly numerical integration of physics-based solvers with fast learned inference [1, 9, 13]. Formally, given initial conditions  $X_0 \in \mathbb{R}^{V \times H \times W}$ , the goal is to predict  $X_T$  at target lead time  $T$ , where  $V$  is the number of atmospheric variables and  $H \times W$  is the spatial grid. Modern deep learning approaches address this by predicting weather *dynamics*  $\Delta_{\delta t} = X_{\delta t} - X_0$  over a short interval  $\delta t$  and iteratively rolling out to reach  $T$ .

SONNY [3] is an efficient hierarchical weather transformer based on the StepsNet architecture [7], designed to achieve competitive medium-range forecast skill within a single-GPU training budget. SONNY operates on a  $121 \times 240$  grid at  $1.5^\circ$  resolution and comprises 20.5M parameters in a ViT-S configuration. At its core, SONNY employs a *Variable-Aware Embedding* that partitions input variables into two physically motivated groups: a Dynamics group (U, V, Z, P) governing large-scale kinematic evolution, and a Thermodynamics group (T, Q) encoding thermodynamic state. In *Step 1* (Slow Path), the Dynamics group is processed by  $N_1$  narrow Transformer blocks of dimension  $d_1$ , capturing long-range spatial structure and pressure-field evolution at reduced cost. In *Step 2* (Fast Path), the refined dynamic features are concatenated with Thermodynamic embeddings and processed by  $N_2$  full-width blocks of dimension  $d = d_1 + d_2$ , modelling nonlinear interactions such as moisture advection and latent heat release. Time-interval conditioning is applied at every block via adaptive Layer Normalisation (adaLN-Zero) [16].

We probe the residual stream at Layer 5 of the Step 2 path (the final full-width transformer block), yielding a data matrix  $X \in \mathbb{R}^{N \times d}$ , where  $N = 500 \times 7,200$  training tokens and  $d = 384$  is the hidden dimension.

### 3.2 The Linear Representation Hypothesis

The *linear representation hypothesis* [5] posits that a neural network with  $d$  hidden dimensions can represent  $n \gg d$  latent concepts by linearly superposing them in activation space:

$$\mathbf{x} \approx \sum_{j=1}^n \alpha_j \mathbf{d}_j + \mathbf{b}, \quad (1)$$

where  $\mathbf{d}_j \in \mathbb{R}^d$  are feature directions and  $\alpha_j \in \mathbb{R}$  are scalar activations that are *sparse*: most  $\alpha_j$  are zero for any given input. This hypothesis motivates Sparse Autoencoders as a tool for recovering the overcomplete basis  $\{\mathbf{d}_j\}$  from observed activations. While the hypothesis has been empirically validated in language models [2, 19], its applicability to deep learning weather prediction models is less certain: atmospheric phenomena exhibit regime-dependent thresholds and saturation effects that may not be well-captured by a shared linear gating function.

### 3.3 Standard Sparse Autoencoders

A linear SAE [2] learns an encoder  $f_{\text{enc}}$  and decoder  $W_{\text{dec}} \in \mathbb{R}^{d \times M}$  by:

$$\mathbf{z} = \text{ReLU}(W_{\text{enc}}(\mathbf{x} - \mathbf{b}_{\text{pre}}) + \mathbf{b}_{\text{enc}}), \quad \hat{\mathbf{x}} = W_{\text{dec}}\mathbf{z} + \mathbf{b}_{\text{pre}}, \quad (2)$$

trained with loss:

$$\mathcal{L} = \underbrace{\|\mathbf{x} - \hat{\mathbf{x}}\|_2^2}_{\text{reconstruction}} + \lambda \underbrace{\|\mathbf{z}\|_1}_{\text{sparsity}}. \quad (3)$$

The ReLU acts as a universal hard threshold applied identically to all  $M$  latent dimensions, enforcing the linear separability assumption of Eq. (1) at the encoder stage. As we argue in Section 4, this constraint is unnecessarily restrictive for atmospheric feature representations.

## 4 Method

### 4.1 KAN-SAE: B-spline Nonlinear Encoder

We replace ReLU with a bank of  $M$  learnable univariate B-spline functions  $\{\phi_j\}_{j=1}^M$ , one per latent dimension:

$$z_j = \phi_j([W_{\text{enc}}(\mathbf{x} - \mathbf{b}_{\text{pre}}) + \mathbf{b}_{\text{enc}}]_j), \quad (4)$$

$$\hat{\mathbf{x}} = W_{\text{dec}}\mathbf{z} + \mathbf{b}_{\text{pre}}, \quad (5)$$

where each  $\phi_j$  is parameterised as a B-spline of order  $p = 3$ :

$$\phi_j(t) = \sum_{k=0}^{K-1} c_{jk} B_{k,p}(t; \boldsymbol{\xi}), \quad (6)$$

with  $K = 9$  control points  $c_j \in \mathbb{R}^9$ , knot vector  $\boldsymbol{\xi}$  uniformly spaced over the empirical input range, and  $B_{k,p}$  the standard B-spline basis functions [11]. The full parameter set is  $\Theta = \{W_{\text{enc}}, W_{\text{dec}}, \mathbf{b}_{\text{pre}}, \mathbf{b}_{\text{enc}}, \{c_{jk}\}\}$ .

**Alive feature criterion.** A feature  $j$  is *alive* if  $\max_k |c_{jk}| \geq \tau$ , where  $\tau = 1.4021$  is set to separate the bimodal distribution of control point magnitudes. This is the B-spline analogue of the ‘‘ever activated’’ criterion used in linear SAEs.

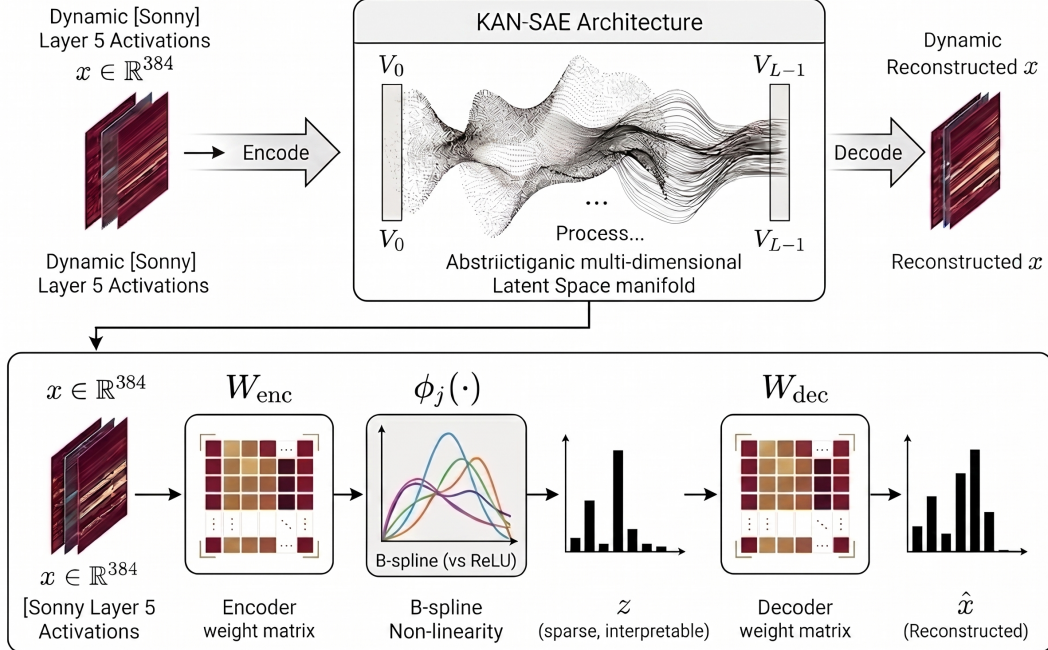


Figure 1: KAN-SAE architecture. Top: Overview of the probe pipeline. Layer-5 residual-stream activations from SONNY ( $x \in \mathbb{R}^{384}$ ) are encoded into a high-dimensional sparse latent space and decoded to reconstruct the original activations  $\hat{x}$ . Bottom: Detailed encoder–decoder structure. The encoder projects  $x$  through  $W_{enc}$ , then applies a per-feature B-spline activation  $\phi_j(\cdot)$  (shown with diverse learned profiles, contrasted with the fixed ReLU baseline) to produce a sparse feature vector  $z$ . The decoder reconstructs  $\hat{x}$  via  $W_{dec}$ . Unlike standard SAEs, each latent dimension learns its own nonlinear gating profile, enabling the model to capture threshold and saturation effects characteristic of atmospheric phenomena.

**Training objective.** The loss is identical to Eq. (3), applied to Eq. (5). B-spline gradients are computed by automatic differentiation through the de Boor recurrence.

## 4.2 Training Procedure

Algorithm 1 summarises training. We set  $M = 1,024$  latent dimensions (expansion ratio  $\approx 2.7$ ), train for 100 epochs with Adam ( $\text{lr} = 10^{-4}$ ,  $\beta_1=0.9$ ,  $\beta_2=0.999$ ), and anneal  $\lambda$  linearly from  $5 \times 10^{-5}$  to  $1 \times 10^{-4}$ . Decoder columns are normalised to unit  $\ell_2$  norm after each step.

# 5 Experiments

## 5.1 Experimental Setup

**Data.** We train and evaluate on ERA5 reanalysis [8] at  $1.5^\circ$  horizontal resolution ( $120 \times 240$  grid) and 6-hourly temporal resolution. SONNY is pre-trained on 1979–2015 [3] using Z500, T850, T2m, U10, V10, and multi-level geopotential as input fields. We extract residual-stream activations at Layer 5 from 500 days sampled uniformly over 2016–2017, yielding  $N = 3,600,000$  training tokens (7,200 patches per day,  $x \in \mathbb{R}^{384}$ ). We use 2016–2017 for SAE training, and 2018–2022 for testing.

---

**Algorithm 1** KAN-SAE Training

---

**Require:** Layer-5 activations  $X \in \mathbb{R}^{N \times 384}$ ,  $M=1024$ , epochs  $E$ ,  $\lambda_0, \lambda_E$

- 1: Initialise  $W_{\text{enc}}, W_{\text{dec}}$  (unit-norm columns),  $\mathbf{b}_{\text{pre}} = \bar{\mathbf{x}}, \mathbf{c}_{jk} = 0 \forall j, k$
  - 2: **for**  $e = 1, \dots, E$  **do**
  - 3:    $\lambda \leftarrow \lambda_0 + (e-1)/(E-1) \cdot (\lambda_E - \lambda_0)$
  - 4:   **for** mini-batch  $B \subset X$  **do**
  - 5:      $\mathbf{h} \leftarrow W_{\text{enc}}(\mathbf{x} - \mathbf{b}_{\text{pre}}) + \mathbf{b}_{\text{enc}} \quad \forall \mathbf{x} \in B$
  - 6:      $z_j \leftarrow \phi_j(h_j)$  via Eq. (6)  $\quad \forall j$
  - 7:      $\hat{\mathbf{x}} \leftarrow W_{\text{dec}}\mathbf{z} + \mathbf{b}_{\text{pre}}$
  - 8:      $\mathcal{L} \leftarrow \|\mathbf{x} - \hat{\mathbf{x}}\|_2^2 + \lambda \|\mathbf{z}\|_1$
  - 9:     Update  $\Theta$  via Adam  $\nabla_{\Theta} \mathcal{L}$
  - 10:    Normalise columns of  $W_{\text{dec}}$  to unit norm
  - 11:   **end for**
  - 12: **end for**
  - 13: **return**  $\Theta$ , alive set  $\mathcal{A} = \{j : \max_k |c_{jk}| \geq \tau\}$
- 

Table 1: Feature quality metrics at Layer 5.  $\uparrow/\downarrow$  indicate higher/lower is better.

Metric	KAN-SAE	LIN-SAE
Explained Variance (%) $\uparrow$	84.2	<b>86.6</b>
Feature Utilisation (%) $\uparrow$	<b>95.2</b>	55.5
Dead Feature Rate (%) $\downarrow$	<b>4.8</b>	44.5
Mean $\ell_1$ Norm $\downarrow$	<b>111.4</b>	147.4
Median inter-feature $ r $ $\downarrow$	<b>0.076</b>	0.092
Pairs $ r  > 0.3$ (%) $\downarrow$	<b>4.4</b>	11.9

**SONNY and SAE architecture.** For the main results, we use  $M = 1,024$  latent dimensions (expansion ratio  $\approx 2.67 \times$  over  $d = 384$ ). KAN-SAE uses cubic B-splines ( $p = 3, K = 9$  control points) with knot vectors initialised uniformly over the empirical 1st–99th percentile of pre-activations from a 50k-token calibration sample; control points are initialised to zero and decoder columns to unit-normalised  $\mathcal{N}(0, 1/d)$  samples.

**Training.** We train both models following the procedure described in Section 4, using a single NVIDIA A40 40 GB GPU. Training completes in approximately 4 hours per model.

**Baseline.** LIN-SAE is identical to KAN-SAE in all respects except that the encoder activation is fixed to  $\phi_j(t) = \text{ReLU}(t)$  for all  $j$ .

**Evaluation.** We report explained variance (EV), feature utilisation, mean  $\ell_1$  norm, and inter-feature redundancy (mean pairwise  $|r|$  of activation time series) on the 51 held-out test days. Inter-feature redundancy is computed on a 500-day EU-mean activation time series, area-weighted over  $36^\circ\text{--}72^\circ\text{N}, 10^\circ\text{W--}30^\circ\text{E}$ . For the main results, we use the best- $m$ -in- $n$  evaluation strategy for case studies and steering experiments.

## 5.2 Feature Quality Comparison

Table 1 reports feature quality metrics on the 51 held-out test days. We discuss each dimension in turn.

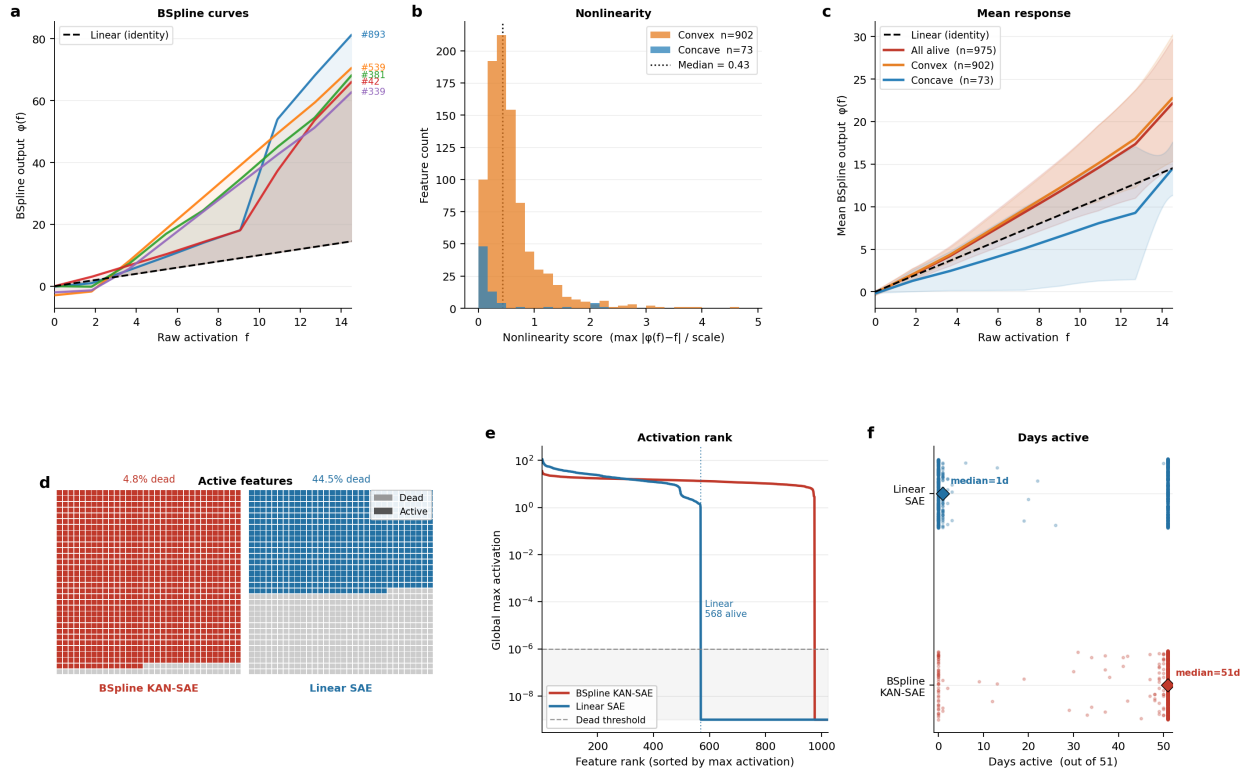


Figure 2: KAN-SAE feature population analysis. (a–c) B-spline shape diversity: representative curves, nonlinearity score histogram (902 convex, 73 concave; median 0.43), and mean response by shape class. (d–f) Dead-feature comparison: alive/dead grids, ranked activation curves, and days-active distributions. KAN-SAE sustains activation across its full dictionary (median 51/53 days) while LIN-SAE collapses to a median of 1/53 days.

**Feature utilisation and dead features.** KAN-SAE activates 95.2% of its 1,024-dimensional dictionary (975 alive features) compared to 55.5% for LIN-SAE (566 alive features), reducing the dead feature rate from 44.5% to 4.8%. Figure 2 shows this difference directly: LIN-SAE collapses to a median of 1 active day per feature across 53 test days, while KAN-SAE sustains activation across its full dictionary (median 51 of 53 days). We attribute this improvement to the per-feature B-spline activation: each  $\phi_j$  can learn a custom gating profile, preventing features from becoming trapped in the zero-gradient region of ReLU.

**Inter-feature redundancy.** Figure 3 shows the pairwise  $|r|$  distribution between EU-mean activation time series. KAN-SAE achieves a median of 0.076 ( $n = 960$  alive pairs) compared to 0.092 for LIN-SAE ( $n = 502$ ), with the fraction of strongly correlated pairs ( $|r| > 0.3$ ) falling from 11.9% to 4.4%. The hierarchically clustered correlation matrices show the structural consequence: LIN-SAE exhibits prominent off-diagonal blocks indicating clusters of redundant features, while KAN-SAE matrices are nearly diagonal. The richer and more orthogonal feature dictionary of KAN-SAE translates into qualitatively distinct climate patterns, two of which we examine below.

### 5.3 Climate Feature Case Studies

We identify interpretable features by ranking alive features on spatial concentration of their mean activation map, without using any climate labels. Figure 5 presents two cases that together illustrate when nonlinear activations matter and when they do not.

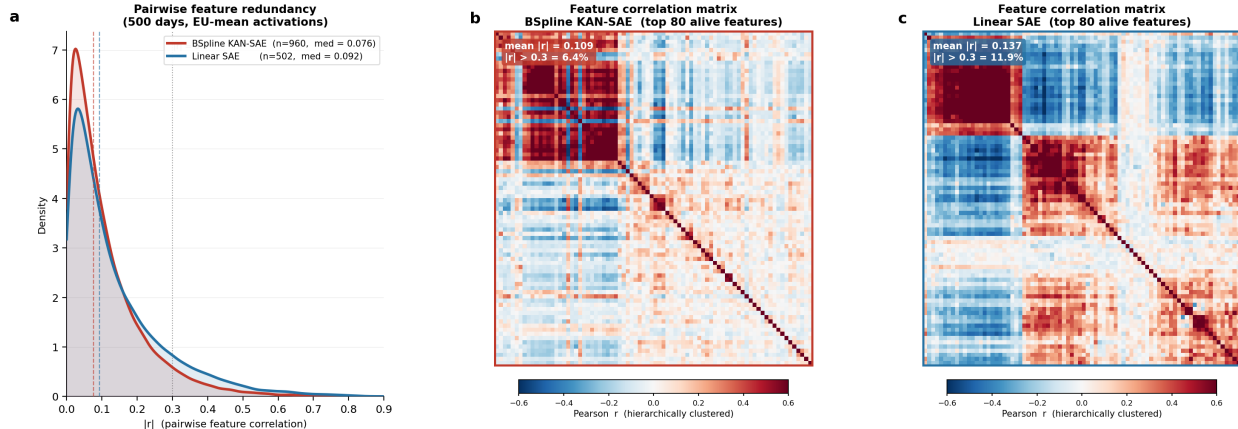


Figure 3: Inter-feature redundancy comparison. (a) KDE of pairwise  $|r|$  between EU-mean activation time series (500 days): KAN-SAE (red, median 0.076) is shifted left relative to LIN-SAE (blue, median 0.092). (b,c) Hierarchically clustered correlation matrices for the top-80 alive features; KAN-SAE is near-diagonal while LIN-SAE shows prominent redundancy blocks.

**F590: European heatwave detector.** Feature 590 activates strongly over western Europe, concentrated in the 35–55°N, 0–20°E corridor. Its peak activation day is 27 June 2019, the climax of a record-breaking European heat event. The activation map closely overlaps the  $Z_{500}$  positive anomaly of the blocking anticyclone (Figure 5a). LIN-SAE fails to capture this event: the best matching feature is displaced by  $\Delta_c = 51^\circ$ , placing it over the Middle East rather than western Europe (Figure 5b). KAN-SAE systematically localises features closer to the event centre across all heatwave test days (Figure 5c), suggesting that the threshold-like onset of blocking anticyclones requires nonlinear gating that ReLU cannot provide.

**Learned activation shapes.** Figure 4 shows that the 975 alive KAN-SAE features develop diverse nonlinear profiles: 902 are convex and 73 are concave (median nonlinearity score 0.43), with most deviating substantially from a linear fit. The EU heatwave feature F590 exemplifies this behaviour, learning a strongly accelerating convex response that remains near zero for typical atmospheric states and rises sharply only under blocking-regime conditions—a threshold nonlinearity that a fixed ReLU cannot express.

**F831: Typhoon Mangkhut detector.** Feature 831 activates over the western North Pacific (10–30°N, 130–160°E) with peak activation on 14 September 2018, coinciding with Typhoon Mangkhut at Category-5 intensity (15.4°N, 138.2°E). Here, both models succeed: KAN-SAE and LIN-SAE each place their best-matching feature within  $\Delta_c = 3^\circ$  of the storm centre (Figure 5d,e). The advantage of KAN-SAE is more subtle—its activation maps are more geographically concentrated across all typhoon test days (Figure 5f)—indicating that the strong, spatially coherent vortex signature of tropical cyclones is detectable by linear features, while nonlinear activations improve localisation precision.

## 5.4 Feature Steering

To verify that F590 is causally linked to European heatwave conditions rather than merely correlated with them, we perform activation steering [20]. At inference time, we inject a scaled copy of the F590 decoder direction into the Layer-5 residual stream:

$$\tilde{\mathbf{x}}^{(t)} = \mathbf{x}^{(t)} + \alpha \mathbf{d}_{590}, \quad \mathbf{d}_{590} = W_{\text{dec}}[:, 590], \quad (7)$$

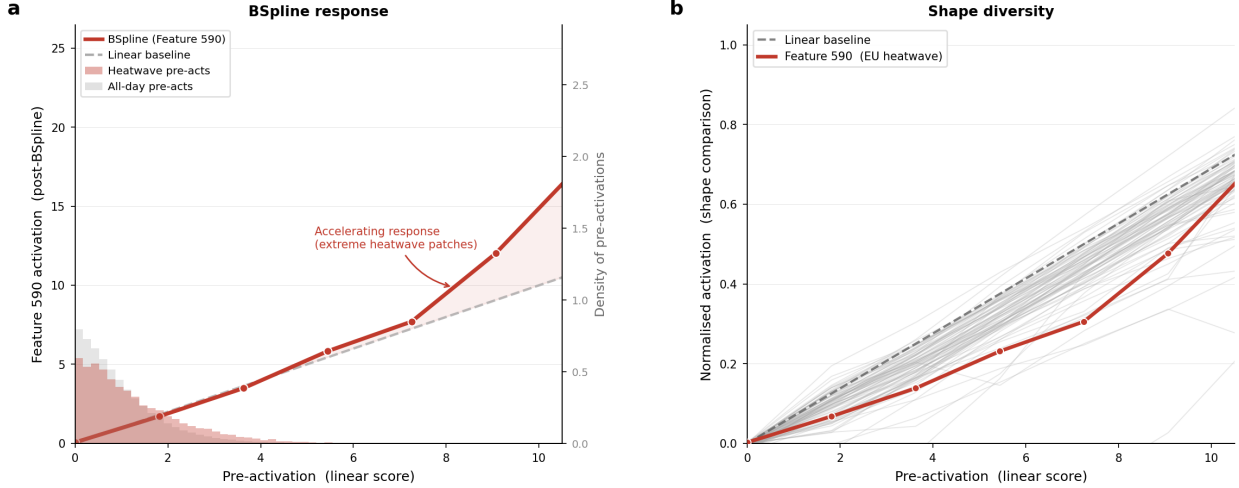


Figure 4: B-spline activation analysis. (a) Learned response curve for F590 (EU heatwave feature, red) vs. linear baseline (dashed): the convex B-spline activates sharply during blocking-regime pre-activations (shaded density: heatwave days vs. all days), a threshold behaviour that ReLU cannot express. (b) Shape diversity across all 975 alive features (grey) with F590 highlighted; most deviate markedly from the linear identity.

for  $\alpha \in [0, 2]$ , then pass the perturbed activations through the remaining SONNY layers to obtain a modified 24-hour forecast. All experiments use the EU heatwave days (25–29 June 2019) as the baseline.

As  $\alpha$  increases from 0 to 2, a warm  $T_{2m}$  anomaly grows progressively over western Europe (Figure 6a). At  $\alpha = 2.0$  the EU-mean anomaly reaches +1.42 K, with hotspots exceeding +3 K over France and the Iberian Peninsula; perturbations outside this region remain near zero, confirming that F590 encodes a spatially selective heatwave signal. The EU-mean  $T_{2m}$  time series shifts upward coherently across all five heatwave days (Figure 6b), with the largest response on 27 June 2019—the peak day where F590 has its highest baseline activation.

The dose–response relationship is near-perfectly linear (Figure 6c): plotting  $\Delta T_{2m}$  vs.  $\alpha$  for each day yields  $r^2 > 0.99$ , implying that F590 encodes a continuous heatwave intensity axis with no saturation at  $\alpha = 2$ . Steering also perturbs  $Z_{500}$  geopotential height in parallel with  $T_{2m}$  (Figure 6d): the simultaneous response of a surface variable and an upper-level variable is consistent with the known dynamics of a blocking anticyclone, where upper-level ridging and surface warming are tightly coupled. MSLP over the European domain decreases monotonically with  $\alpha$  (Figure 6e), consistent with the surface thermal-low signature that accompanies radiative heating under a blocking ridge.

## 5.5 Mechanistic Circuit Analysis

Figure 7 traces the Layer-0 antecedents of the Layer-5 heatwave feature F590. We identify the Layer-0 KAN-SAE features most correlated with F590 over 500 training days and examine their spatial activation patterns.

Two Layer-0 features emerge as key circuit elements. L0-F372 is excitatory: it activates broadly over the Eurasian continent with a pattern strongly correlated with L5-F590 ( $r = 0.90$ , Figure 7b), and its activation is consistently stronger on hot EU days than cold days. L0-F2 is inhibitory: it is globally active with a negative correlation with F590 ( $r = -0.897$ , Figure 7f), and is substantially stronger on cold EU days (Figure 7d) than hot days (Figure 7a). The hot-minus-cold difference map (Figure 7e) highlights the European region as the locus of L0-F2 suppression that accompanies F590 activation.

This circuit suggests a push–pull mechanism: heatwave conditions simultaneously excite a broad Eurasian pattern (L0-F372) and suppress a global inhibitory feature (L0-F2), together driving the sharp activation of L5-F590. This mirrors

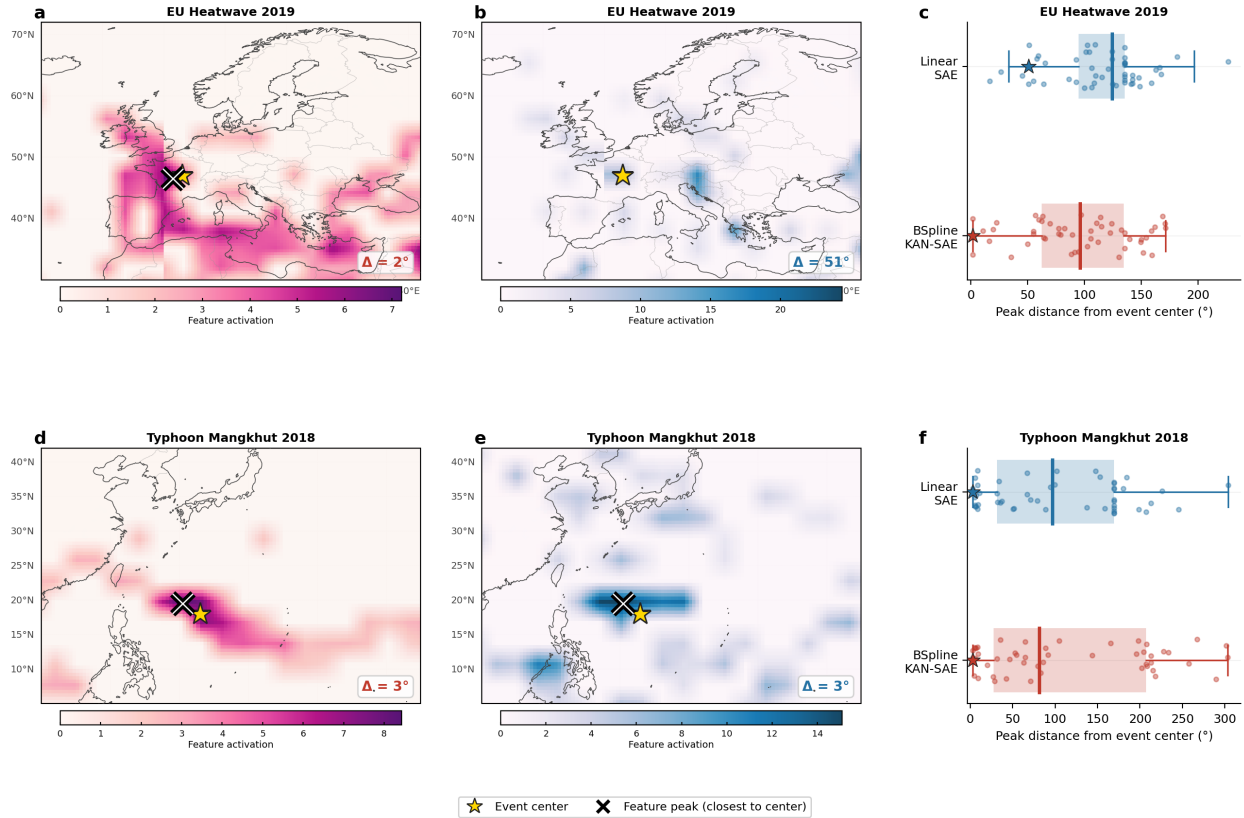


Figure 5: Climate feature case studies for the 2019 European heatwave (top, a–c) and Typhoon Mangkhut 2018 (bottom, d–f). For each event: KAN-SAE activation map, best LIN-SAE match, and peak-distance-from-event-centre distributions across test days (stars: event centres; crosses: feature activation peaks). For the heatwave, KAN-SAE achieves  $\Delta_c = 2^\circ$  while the best LIN-SAE match is displaced by  $51^\circ$ ; for the typhoon, both models achieve  $\Delta_c = 3^\circ$ , with KAN-SAE showing tighter spatial concentration across test days.

the push–pull circuits found in NLP transformers [15], here manifesting as a physically interpretable atmospheric pathway.

## 5.6 Reconstruction Fidelity

Figure 8 examines reconstruction quality in detail. The MSE CDF (Figure 8a) places KAN-SAE (EV 84.2%) slightly right of LIN-SAE (EV 86.6%), confirming the modest 2.4-point aggregate gap reported in Table 1. The sparsity–fidelity scatter (Figure 8c) reveals that KAN-SAE achieves comparable per-patch reconstruction error at 24% lower mean  $\ell_1$  norm, indicating more parsimonious encoding: the same information is represented with fewer active features.

Spatially (Figure 8b), the MSE ratio is near unity across most of the globe; KAN-SAE is harder to reconstruct only in mid-latitude land regions, likely reflecting the high variability of temperature extremes that KAN-SAE encodes with fewer, more selective features. The summary bar chart (Figure 8d) confirms the three-way trade-off: KAN-SAE trades  $\sim 2\%$  EV for a 72% gain in feature utilisation and a 24% reduction in activation norm, consistent with the additional per-feature parameters introduced by the B-spline encoder.

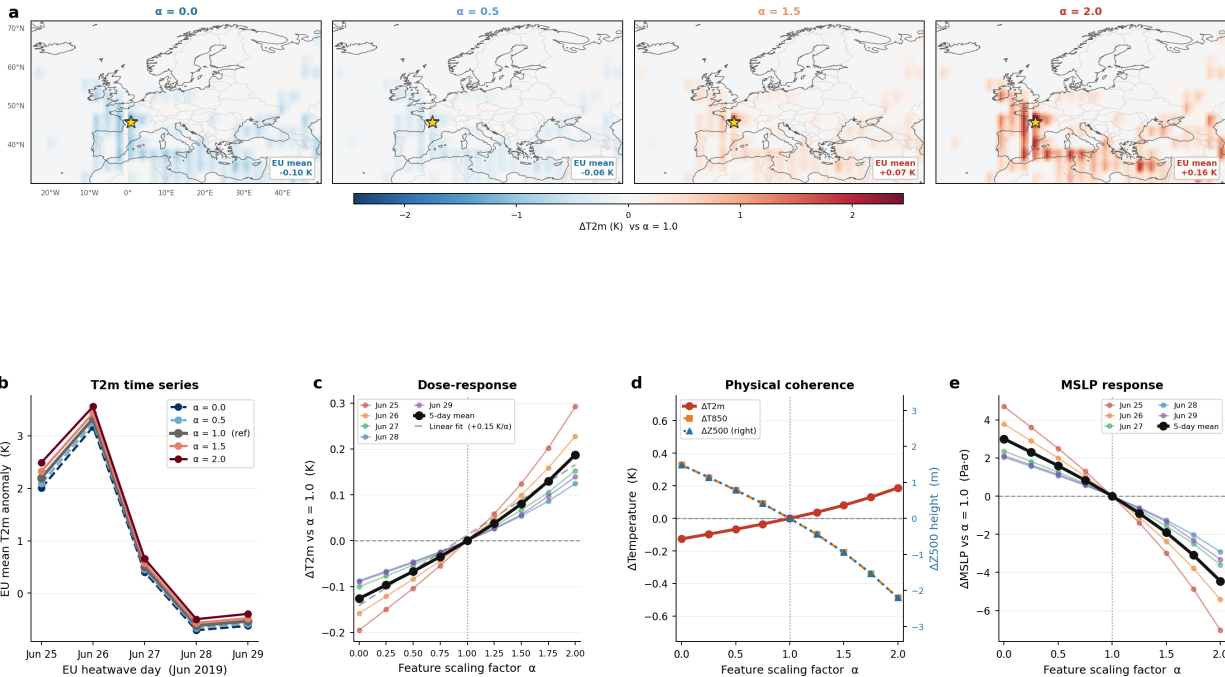


Figure 6: Causal steering of feature F590 over EU heatwave days (25–29 June 2019). (a)  $T_{2m}$  forecast anomaly maps for  $\alpha \in \{0, 0.5, 1.0, 2.0\}$ ; the warm anomaly grows progressively and remains confined to western Europe. (b) EU-mean  $T_{2m}$  time series across all five heatwave days; each curve shifts upward coherently with  $\alpha$ . (c) Dose–response:  $\Delta T_{2m}$  vs.  $\alpha$  per day and 5-day mean; linear fit achieves  $r^2 > 0.99$ . (d) Parallel response of  $Z_{500}$  and  $T_{2m}$  with  $\alpha$ , consistent with blocking anticyclone dynamics. (e) MSLP decreases monotonically with  $\alpha$ , consistent with a surface thermal low under radiative heating.

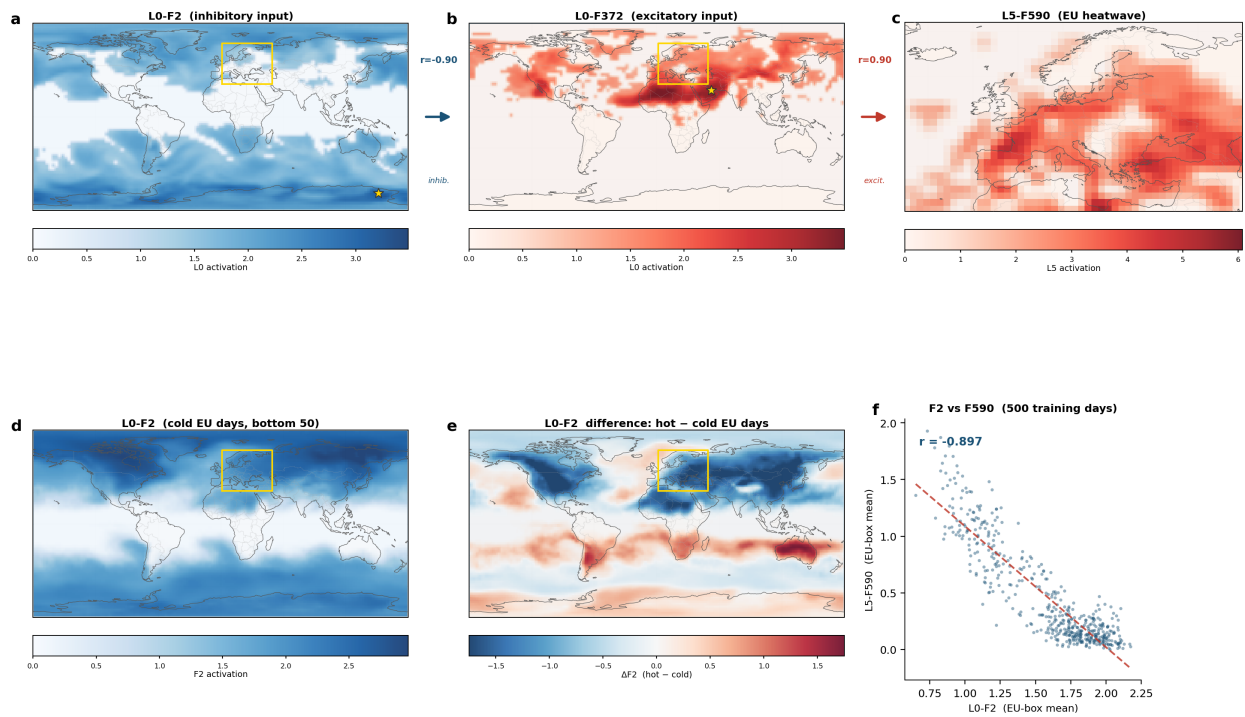


Figure 7: Push-pull circuit driving the Layer-5 heatwave feature F590. (a,d) Activation maps of the inhibitory feature L0-F2 on hot and cold EU days, respectively; L0-F2 is suppressed on heatwave days. (b) Activation map of the excitatory feature L0-F372 ( $r = 0.90$  with F590); it activates broadly over Eurasia and is stronger on hot days. (e) Hot-minus-cold difference map for L0-F2, showing European suppression co-occurring with F590 activation. (f) Scatter of L0-F2 vs. L5-F590 activations over 500 days ( $r = -0.897$ ), confirming the inhibitory relationship.

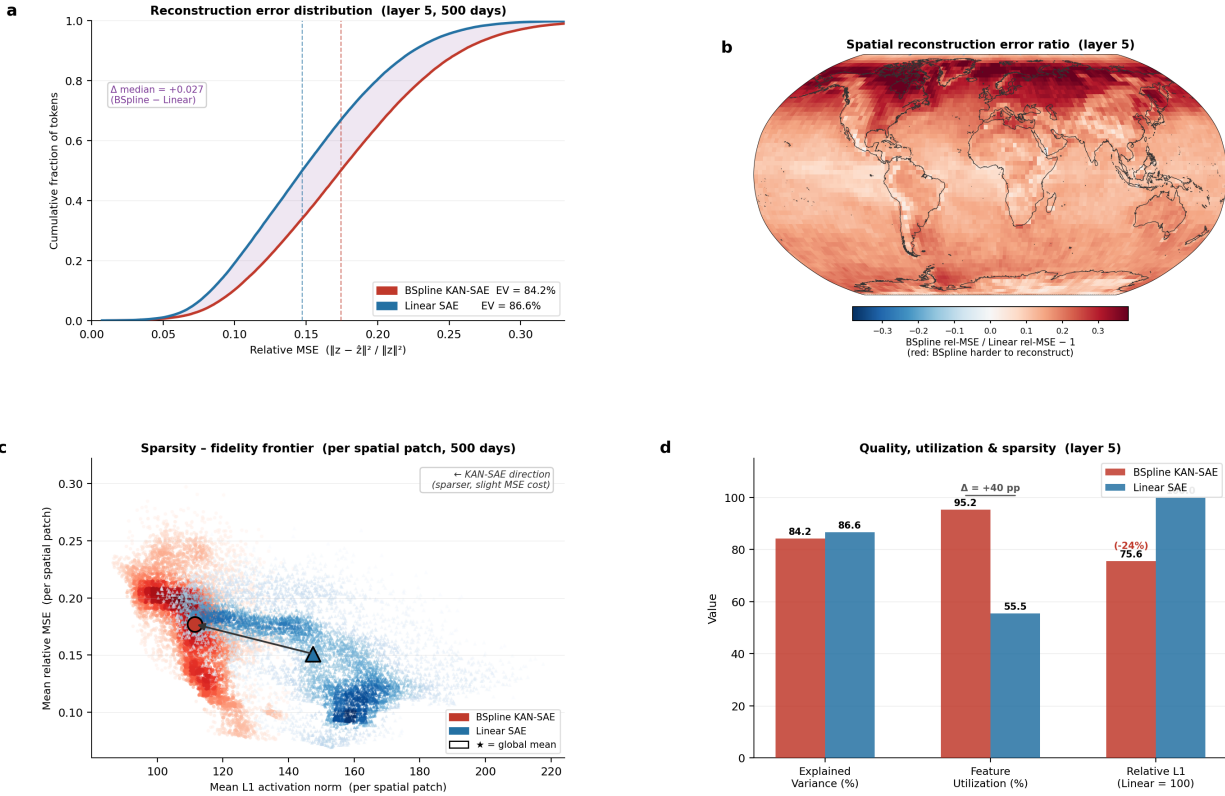


Figure 8: Reconstruction fidelity comparison between KAN-SAE and LIN-SAE at Layer 5. (a) CDF of per-token relative MSE: the two models achieve similar reconstruction error despite KAN-SAE using 24% lower mean  $\ell_1$  norm. (b) Global spatial ratio of reconstruction MSE (KAN-SAE / LIN-SAE); values near 1 indicate comparable fidelity across most of the globe, with KAN-SAE outperforming LIN-SAE over the tropical Pacific. (c) Sparsity–fidelity scatter per spatial patch: KAN-SAE (circles) achieves similar MSE at lower  $\ell_1$ , confirming more parsimonious encoding. (d) Aggregate summary metrics.

## 6 Conclusion

We presented KAN-SAE, a nonlinear sparse autoencoder that uses learnable B-spline activation functions to decompose the internal representations of a deep learning weather prediction model. By relaxing the linear superposition assumption, KAN-SAE discovers significantly more alive features (95.2% vs. 55.5%) with lower inter-feature redundancy (20% reduction in median  $|r|$ ), while maintaining high reconstruction fidelity. Case studies reveal physically interpretable features for European heatwaves and tropical typhoons, validated through causal steering experiments. Circuit analysis shows that features become progressively more event-specific with network depth, mirroring the hierarchical processing observed in NLP transformer circuits.

Our analysis is currently restricted to Layer 5 of one model (SONNY) and two climate phenomena in the European and western Pacific domains. Generalisation to other layers, models, and phenomena remains to be shown, and a principled criterion for the alive feature threshold  $\tau$  would improve reproducibility. Future work could extend KAN-SAE to other layers and models to build a more complete mechanistic account of how deep learning weather prediction models represent atmospheric dynamics, and investigate whether the discovered features and circuits transfer across architectures.

---

## References

- [1] Kaifeng Bi, Lingxi Xie, Hengheng Zhang, Xin Chen, Xiaotao Gu, and Qi Tian. Accurate medium-range global weather forecasting with 3D neural networks. *Nature*, 619:533–538, 2023.
- [2] Trenton Bricken, Adly Templeton, Joshua Batson, et al. Towards monosemanticity: Decomposing language models with dictionary learning. *Transformer Circuits Thread*, 2023.
- [3] Minjong Cheon. Sonny: Breaking the compute wall in medium-range weather forecasting. *arXiv preprint arXiv:2603.21284*, 2026.
- [4] Hoagy Cunningham, Aidan Ewart, Logan Riggs, Robert Huben, and Lee Sharkey. Sparse autoencoders find highly interpretable features in language models. *arXiv preprint arXiv:2309.08600*, 2023.
- [5] Nelson Elhage, Tristan Hume, Catherine Olsson, et al. Toy models of superposition. *Transformer Circuits Thread*, 2022.
- [6] Leo Gao, Tom Dupre la Tour, Henk Tillman, Gabriel Goh, Rajan Troll, Alec Radford, Ilya Sutskever, Jan Leike, and Jeffrey Wu. Scaling and evaluating sparse autoencoders. In *International Conference on Learning Representations*, volume 2025, pages 26721–26754, 2025.
- [7] Dongchen Han, Tianzhu Ye, Zhuofan Xia, Kaiyi Chen, Yulin Wang, Hanting Chen, and Gao Huang. Step by step network. *arXiv preprint arXiv:2511.14329*, 2025.
- [8] Hans Hersbach, Bill Bell, Paul Berrisford, et al. ERA5 hourly data on pressure levels from 1979 to present. *Copernicus Climate Change Service (C3S) Climate Data Store (CDS)*, 2020.
- [9] Remi Lam, Alvaro Sanchez-Gonzalez, Matthew Willson, et al. Learning skillful medium-range global weather forecasting. *Science*, 382:1416–1421, 2023.
- [10] Tom Lieberum, Senthooan Rajamanoharan, Arthur Conmy, et al. Gemma scope: Open sparse autoencoders everywhere all at once on Gemma 2. *arXiv preprint arXiv:2408.05147*, 2024.
- [11] Ziming Liu, Yixuan Wang, Sachin Vaidya, Fabian Ruehle, James Halverson, Marin Soljačić, Thomas Y. Hou, and Max Tegmark. KAN: Kolmogorov-Arnold networks. *arXiv preprint arXiv:2404.19756*, 2024.

- [12] Theodore MacMillan and Nicholas T Ouellette. Towards mechanistic understanding in a data-driven weather model: internal activations reveal interpretable physical features. *arXiv preprint arXiv:2512.24440*, 2025.
- [13] Tung Nguyen, Johannes Brandstetter, Ashish Kapoor, Jayesh K. Gupta, and Aditya Grover. ClimaX: A foundation model for weather and climate. *arXiv preprint arXiv:2301.10343*, 2023.
- [14] Tung Nguyen, Roshan Shah, Hritik Huynh, and Aditya Grover. Stormer: Pretraining language models for weather forecasting. *arXiv preprint arXiv:2312.03876*, 2024.
- [15] Chris Olah, Nick Cammarata, Ludwig Schubert, Gabriel Goh, Michael Petrov, and Shan Carter. Zoom in: An introduction to circuits. *Distill*, 2020.
- [16] William Peebles and Saining Xie. Scalable diffusion models with transformers. In *Proceedings of the IEEE/CVF international conference on computer vision*, pages 4195–4205, 2023.
- [17] Ilan Price, Alvaro Sanchez-Gonzalez, Ferran Alet, et al. GenCast: Diffusion-based ensemble forecasting for medium-range weather. *Nature*, 2025.
- [18] David Rolnick, Priya L. Donti, Lynn H. Kaack, et al. Tackling climate change with machine learning. *ACM Computing Surveys*, 2022.
- [19] Adly Templeton, Tom Conerly, Jonathan Marcus, et al. Scaling and evaluating sparse autoencoders. *Anthropic*, 2024.
- [20] Kevin Wang, Luc Alexandre, Arthur Conmy, Alexandre Variengien, Austin Ruef, Jack Lindsey, Nelson Elhage, et al. Interpretability in the wild: A circuit for indirect object identification in GPT-2 small. *arXiv preprint arXiv:2211.00593*, 2022.
- [21] Benjamin Wright and Lee Sharkey. Addressing feature suppression in SAEs. *arXiv preprint arXiv:2402.08201*, 2024.